nature communications

Article

https://doi.org/10.1038/s41467-024-53678-4

A general flame aerosol route to kinetically stabilized metal-organic frameworks

Received: 28 June 2024

Accepted: 17 October 2024

Shuo Liu[1,2], Chaochao Dun[2,6], Feipeng Yang[3], Kang-Lan Tung[1], Dominik Wierzbicki[3,4], Sanjit Ghose[3], Kaiwen Chen[1], Linfeng Chen[2], Richard Ciora[1], Mohd A. Khan[1], Zhengxi Xuan[1,5], Miao Yu[1,5], Jeffrey J. Urban[2,6] & Mark T. Swihart[1,5,6]

Metal-organic frameworks (MOFs) are highly attractive porous materials with applications spanning the fields of chemistry, physics, biology, and engineering. Their exceptional porosity and structural flexibility have led to widespread use in catalysis, separation, biomedicine, and electrochemistry. Currently, most MOFs are synthesized under equilibrium liquid-phase reaction conditions. Here we show a general and versatile non-equilibrium flame aerosol synthesis of MOFs, in which rapid kinetics of MOF formation yields two distinct classes of MOFs, nano-crystalline MOFs and amorphous MOFs. A key advantage of this far-from-equilibrium synthesis is integration of different metal cations within a single MOF phase, even when this is thermodynamically unfavorable. This can, for example, produce single-atom catalysts and bimetallic MOFs of arbitrary metal pairs. Moreover, we demonstrate that dopant metals (e.g., Pt, Pd) can be exsolved from the MOF framework by reduction, forming nanoclusters anchored on the MOF. A prototypical example of such a material exhibited outstanding performance as a CO oxidation catalyst. This general synthesis route opens new opportunities in MOF design and applications across diverse fields and is inherently scalable for continuous production at industrial scales.

The ultra-high porosity and surface area, chemical diversity, and structural stability of MOFs[1] have led to intense research activity and diverse applications including catalysis[2], gas capture/separation[3,4], biomedicine[5], sensors[6], and atmospheric water harvesting[7]. Over the past 30 years, numerous MOF synthesis methods have been developed (Fig. 1). MOF synthesis typically occurs under near-equilibrium conditions, where the MOF formation is the product of classical nucleation and growth processes. In contrast, a flame aerosol process (also called flame spray pyrolysis) provides non-equilibrium and dynamic reaction conditions, where the material forms in milliseconds via gas-to-particle conversion, nucleating from the vapor phase, or droplet-to-particle conversion, nucleating within aerosol droplets[8,9]. Flame aerosol processes are widely employed for industrial production of powders, such as carbon black and fumed silica, because of their scalability, continuous mode of operation, and relatively low cost[10]. However, the synthesis of MOFs by flame aerosol processes has not been explored. A key challenge is that the high temperature of conventional flame aerosol processes (~2000 °C) is incompatible with the organic linkers in MOFs. Nonetheless, synthesizing MOFs under milder conditions using similar flame-driven non-equilibrium methods holds promise for

---

[1]Department of Chemical and Biological Engineering, University at Buffalo, The State University of New York, Buffalo, NY 14260, USA. [2]The Molecular Foundry, Lawrence Berkeley National Laboratory, Berkeley, CA 94720, USA. [3]National Synchrotron Light Source Ⅱ, Brookhaven National Laboratory, Upton, NY 11973, USA. [4]AGH University of Science and Technology, Faculty of Energy and Fuels, Al. A. Mickiewicza 30, 30-059 Cracow, Poland. [5]RENEW Institute, University at Buffalo, The State University of New York, Buffalo, NY 14260, USA. [6]These authors contributed equally: Chaochao Dun, Jeffrey J. Urban, Mark T. Swihart. e-mail: cdun@lbl.gov; jjurban@lbl.gov; swihart@buffalo.edu

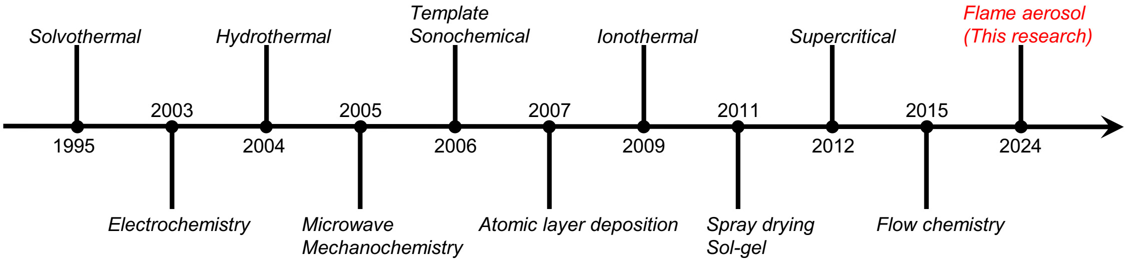

Fig. 1 | Simplified timeline of development of MOF synthesis approaches[52–58].

the fabrication of either nano-crystalline MOFs or amorphous MOFs, as well as the integration of different metal cations within a single MOF phase. Rapid MOF formation and quenching allows trapping of these kinetically stabilized (metastable relative to crystallization, separation into multiple domains, and crystallite growth) structures.

Nano-crystalline MOFs have advantages relative to conventional MOFs in some important cases. A significant aspect of these nano-crystalline MOFs is their high external surface area-to-volume ratio, a direct consequence of their reduced size. This characteristic enhances the accessibility of active sites and reduces transport distances in the characteristic micropores of the MOF crystal structures. Thus, small crystallite size is advantageous for applications requiring efficient catalysis (access to active sites) and gas storage (rapid transport in and out of micropores)[1]. Additionally, the particular surface characteristics of these nano-crystals may lead to enhanced reactivity and selectivity in chemical reactions[11]. Moreover, the higher concentration of structural defects in nano-crystalline MOFs can be beneficial[12]. Efforts to reduce MOF crystal size to the nano-scale have been widespread, with typical nanocrystal MOFs produced in the ~100 nm size range (e.g., an average nanocrystal size of 160 nm for HKUST-1 MOFs). However, achieving sizes below 100 nm remains challenging in many MOF chemistries[13].

In contrast to conventional and nanocrystalline MOFs, an amorphous MOF (also called a MOF glass or disordered MOF) retains the basic building blocks and connectivity of its crystalline counterpart but lacks long-range periodic order[14]. Although the surface area of amorphous MOFs is usually much lower than their crystalline MOF counterparts, their enhanced thermal stability, mechanical flexibility (ductility), optical properties, and ion conductivity are valuable in many fields[15]. For example, ultrahigh gas permeance and selectivity have been demonstrated in membranes based on amorphous MOFs[16]. To date, the majority of amorphous MOFs have been from the ZIF family of materials, which use imidazolate linkers, rather than the polycarboxylate linkers used in most MOFs. These amorphous ZIFs are produced from crystalline ZIFs via post-treatments, such as the application of heat and/or pressure, mechanical milling, or irradiation[17].

While the versatility and potential of nano-crystalline MOFs and amorphous MOFs in a variety of scientific and industrial settings are evident, a direct and general method to prepare them has not previously been available. The rapid, far-from-equilibrium formation process enabled by flame aerosol synthesis promotes the formation of these nano-crystalline MOFs and amorphous MOFs, vastly enhancing the range of MOF chemistries for which they can be produced.

In addition, incorporating single-atom active sites into a MOF matrix is highly desirable in catalysis, to maximize utilization of noble metals, while the MOF provides high surface area and porosity for reactant adsorption and conversion[18]. However, differences in size, preferred oxidation state, and electronegativity between the noble metal dopants and the MOF cations make substitutional doping of noble metals into the MOF framework difficult or impossible. Thus, there are two main strategies for preparing MOF-based single-atom catalysts: (1) substitution of MOF cations by a noble metal in the MOF structure, before or during MOF syntheses; or (2) addition of functional groups in the frameworks, to which single noble metal ions can coordinate[19]. Each of these approaches requires a particular coordination environment or complex post-treatment processes. Thus, a direct and general method to dope single-metal atoms of those metals of greatest interest for catalysis into a MOF matrix is also lacking.

Here, we first report a flame aerosol synthesis method to fabricate MOFs, based on a modified flame aerosol reactor that separates flame chemistry from the particle formation process[20,21]. We demonstrate the universality of this process by producing 9 different nanocrystalline MOFs and 9 different amorphous MOFs, spanning most of the key MOF subfamilies and MOF-like structures (e.g., Prussian blue analogues). We then show that our method enables in-situ incorporation of diverse pairs of elements in a single MOF phase. We demonstrate this universality by doping 4 different single-atom metal sites into different host MOFs. Furthermore, we show that reducing the noble metal component of a bimetallic MOF drives an exsolution process to form highly dispersed metal nanoclusters supported on the MOF. As a prototypical example of the power of this approach, we use exsolved Pt clusters on UiO-66-NH_2 as a CO oxidation catalyst that achieves 100% CO conversion at 130 °C.

Results

Synthesis mechanism

The MOFs were fabricated in a one-step and continuous flame aerosol process, as described in detail in the Methods section (Fig. 2, Supplementary Fig. 1). The liquid precursor containing metal ions, organic linker molecules, and solvent was continuously injected into the flow reactor, while the product was continuously collected downstream. In general, the MOFs formed via a rapid droplet-to-particle conversion route. When the precursor solution was injected into the reactor, it was shear-atomized by a hot, high-velocity gas stream into droplets of a few micrometer diameter[22,23]. Rapid solvent evaporation increased the solute concentration at droplet surface. Thus, assembly of reactants began at the droplet surface, and then the MOF grew inwardly, finally forming a hollow sphere from each droplet[24].

The evaporation of solvent from each micro-droplet occurred in a few milliseconds[25] and subsequent exposure to high temperature took place within a residence time of ~50 ms before solid particles were quenched by N_2 at the reactor exit. This rapid quenching can often trap materials in a metastable state. This rapid MOF formation process can be characterized as a far-from equilibrium, as opposed to the more common MOF crystallization processes such as solvothermal treatment that proceed slowly under near-equilibrium conditions. The fast evaporation and resulting solute concentration increase inherent in the flame aerosol process promotes rapid MOF formation. This can either occur through simultaneous nucleation of multiple crystalline domains within each droplet or result in a disordered framework. The rapid droplet-to-particle conversion in this process typically yields kinetic, rather than thermodynamic, products. In this context, two distinct classes of MOFs, nano-crystalline MOFs and amorphous MOFs can be produced (Fig. 2). The product properties can be varied and optimized by adjusting reaction parameters (e.g., gas flow rates, H_2 to O_2 ratio, precursor flow rate, precursor concentration, and metal ion to linker ratio). However, in this study, to demonstrate the versatility of

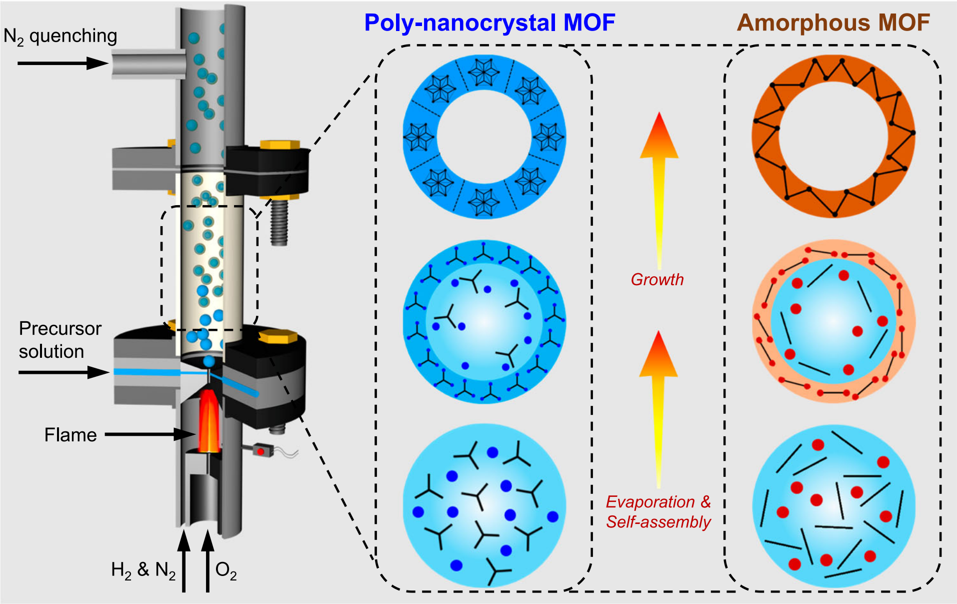

Fig. 2 | Schematic representation of nanocrystal and amorphous MOFs formation in a non-equilibrium flame aerosol process.

the method, all MOFs were synthesized using a common set of synthesis and washing procedures, with only the precursor composition varying (Supplementary Table 1, 2).

Nanocrystal MOFs

A prototypical flame synthesized nanocrystal MOF, Cu HKUST-1 (also known as MOF-199, $Cu_3(BTC)_2$, BTC = 1,3,5-benzenetricarboxylate), is depicted in Fig. 3. This MOF comprised $Cu_2(OAc)_4$ paddlewheel secondary building units interconnected by tridentate BTC ligands[26]. Scanning electron microscopy (SEM) imaging showed the spherical morphology of the MOF particles (Fig. 3a). A series of Cu HKUST-1 MOFs prepared from precursors containing 5 mM, 10 mM, and 20 mM Cu ions under otherwise identical conditions exhibited geometric mean diameters of 365 nm, 420 nm, and 490 nm, respectively, demonstrating that the particle size can tuned to some degree by varying the concentration of the precursor (Supplementary Fig. 2). Transmission electron microscopy (TEM) imaging showed hollow nanoshell structures with thin and uniform walls. The polycrystalline nature of flame-synthesized Cu HKUST-1 was evident, with numerous MOF nanocrystals packed into a dense shell. High-angle annular dark-field scanning transmission electron microscopy (HAADF-STEM) with elemental mapping by energy-dispersive x-ray spectroscopy (EDS) confirmed the presence of Cu, C, and O in the MOF particles. Note that the flame aerosol process produced MOF nanocrystals with a grain size of 20~40 nm, significantly smaller than traditional nanocrystal MOFs that are more often in the 100 nm size range. The abundant grain boundaries in the polycrystalline MOFs may play significant roles in processes such as gas adsorption and diffusion[27].

X-ray diffraction (XRD) confirmed the pure crystalline HUKST-1 structure (Fig. 3b, Supplementary Table 4). However, the peaks were broadened, yielding a crystallite size of 33.4 nm calculated by applying the Scherrer equation to the peak at $2\theta = 11.9°$. The formation of bridging bonds between Cu ions and BTC linkers was confirmed by Fourier transform infrared (FTIR) spectroscopy (Fig. 3c). Two new bands appeared at 1372 and 1544 cm^{-1}, which can be assigned to the symmetric and asymmetric stretches of the coordinated carboxyl groups[28]. The observed shift is attributed to the transition of carboxyl groups from a free state to a metal-ion coordinated state. The presence of the BTC linker was confirmed by hydrogen nuclear magnetic resonance (1H NMR) after digestion of the MOF, confirming that the linker was not altered in the high-temperature synthesis (Fig. 3d). The Cu ions and chemical bonds in BTC were also evident in X-ray photoelectron spectroscopy (XPS) (Supplementary Fig. 3). All evidence corroborates the successful synthesis of HKUST-1. Porosity and surface areas of flame-synthesized Cu HKUST-1 MOFs with different Cu ion concentrations in the precursor solution were quantified by N_2 sorption analysis at 77 K (Fig. 3e, Supplementary Figs. 4 and 5, Supplementary Table 3). The type | isotherm indicated the microporous nature of the flame-synthesized MOFs. For the sample prepared with 60 mM Cu^{2+}, the BET surface area was 1052 m^2/g, and the Langmuir surface area was 1707 m^2/g, comparable to liquid-phase synthesized HKUST-1 MOFs[26,29]. The pore volume plot was estimated by the Horvath-Kawazoe method, showing a uniform pore size distribution from 3 to 6 Å in diameter.

To demonstrate the versatility of the flame aerosol process, we extended this method to fabricate a library of nanocrystalline MOFs, including Cu BDC, Tb PDA, Cu FMA, Ni PBA, Zn BDC-NH_2, Zn BTC, Cu PMA and Cu BTB (Supplementary Table 1, Supplementary Fig. 6a). XRD patterns for all materials showed distinct diffraction peaks at low angles, indicating successful coordination of metal ions onto organic linkers, forming crystalline MOFs (Supplementary Fig. 6b–i, Supplementary Fig. 7). However, all XRD peaks were weaker and broader than in conventional MOFs, consistent with nanocrystal sizes in the range of 5~30 nm (Supplementary Tables 5–12). The SEM images consistently showed sub-micrometer spherical particles for all MOFs (Supplementary Fig. 8), while the TEM images further confirmed the polycrystalline nature of these particles, with MOF nanocrystals packed into hollow nanoshells (Supplementary Fig. 9). In our exploration of MOF synthesis, we observed that metals like Cu, Zn, and Ni tend to form crystalline MOFs more readily. The assembly of MOFs depends on the evaporation rate of the precursor droplets. Methods that decelerate this evaporation, such as reducing the reaction temperature, may favor the formation of crystalline MOFs.

Amorphous MOFs

In some cases, the non-equilibrium droplet-to-particle conversion process was too fast to facilitate the assembly of building units into crystalline MOFs. Instead, it generated a disordered and monolithic framework of metal ions linked by organic molecules (Fig. 2). A prototypical flame-synthesized amorphous MOF, Zr FMA (corresponding to the crystalline MOF known as MOF-801, Zr-fumarate, FMA=Fumaric

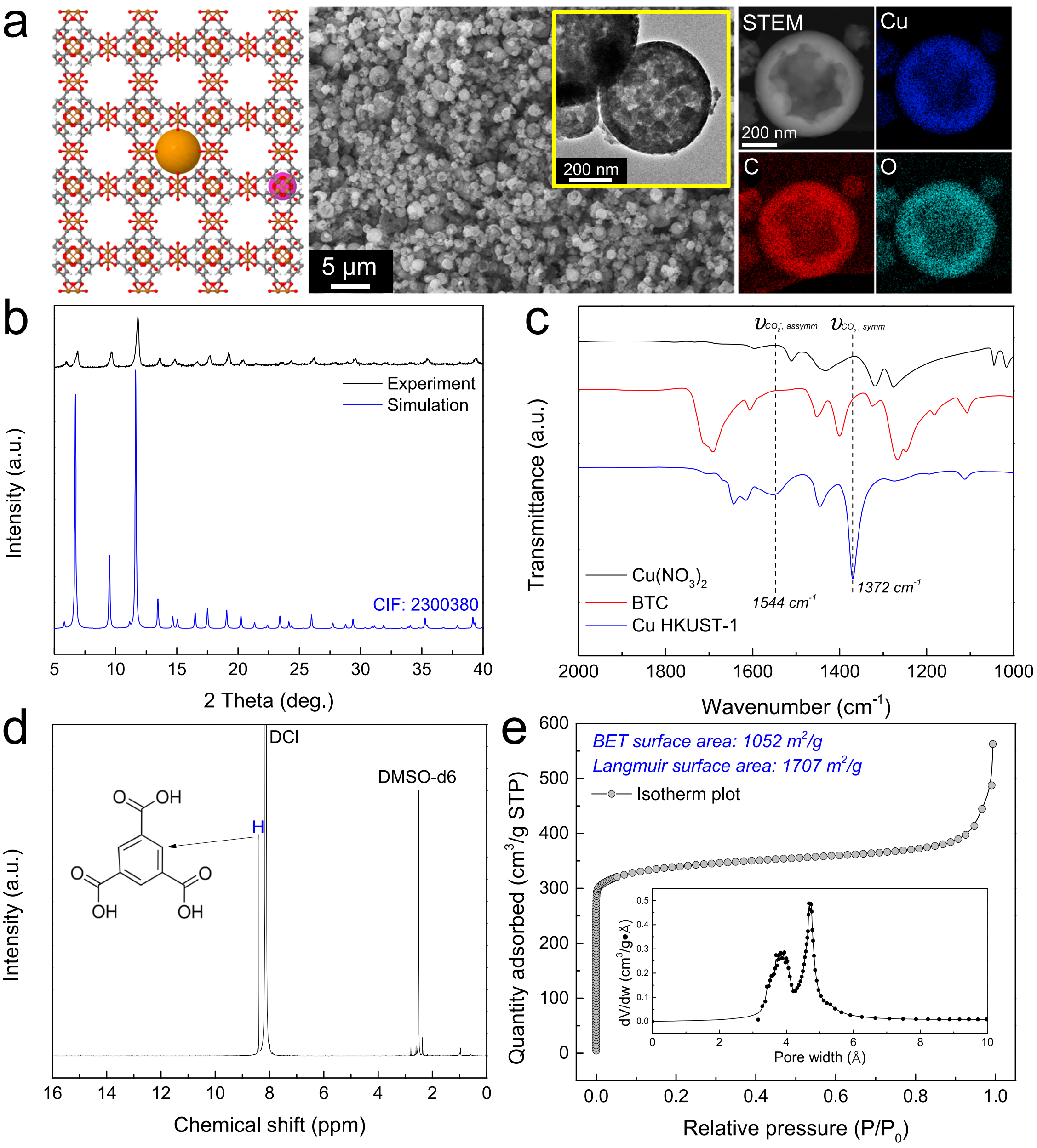

Fig. 3 | Flame-synthesized nanocrystal MOF, Cu HKUST-1. a Structural schematic, SEM, TEM images, and HAADF-STEM and STEM-EDS elemental maps; **b** XRD patterns of experimental and simulated Cu HKUST-1; **c** FTIR spectra of $Cu(NO_3)_2$, BTC ligand, and Cu HKUST-1; **d** ^1H NMR spectrum. The MOF was digested in a mixture of 35% DCl in D_2O and DMSO-d6; **e** N_2 adsorption isotherm plot and Horvath–Kawazoe differential pore volume plot (60 mM Cu^{2+}). Similar characterization results for additional nanocrystal MOFs are shown in Supplementary Figs. 6–9.

acid), is depicted in Fig. 4. This amorphous MOF consisted of Zr nodes interconnected by fumarate ligands without long-range order. SEM imaging showed spherical MOF particles (Fig. 4a). A series of amorphous Zr FMA MOFs prepared from precursors containing 5 mM, 10 mM, and 20 mM Zr ions under otherwise identical conditions exhibited geometric mean diameters of 308 nm, 356 nm, and 399 nm, respectively (Supplementary Fig. 10). TEM images revealed that large particles remained hollow spheres, while many small particles collapsed into solid spheres. Meanwhile, high-resolution TEM (HRTEM) and fast-Fourier-transform (FFT) patterns revealed the disordered arrangement of building blocks, which may enhance interconnectivity of micropores[16]. HAADF-STEM elemental maps confirmed the uniform distribution of Zr, C, and O (Supplementary Fig. 11).

The XRD pattern of the amorphous Zr FMA exhibited a broad peak at $2\theta = 8.6°$ (Fig. 4b), corresponding to a d-spacing of 10.1 Å. Similar broad XRD diffraction peaks have also been observed in other reported amorphous MOFs[14,30,31]. The peak position aligned with the first diffraction peak of crystalline Zr MOF-801, indicating the presence of some degree of local order. The coherently scattering domain size was estimated to be 3.4 nm using the Scherrer equation. This result was corroborated by X-ray total scattering experiments, revealing no sharp Bragg peaks in the calculated static structure factor S(Q) (Supplementary Fig. 12). A Fourier transform of S(Q) yielded the pair distribution function (PDF), which further demonstrated the short-range ordered structure of amorphous Zr FMA (Fig. 4c). Similar PDF patterns revealing short-range order were observed for other reported amorphous MOFs[16,32]. Major peaks below 5 Å corresponded to the distance of nearest neighbor atom pairs, with no evident peaks at medium-range or longer distances. Meanwhile, the PDF over a range of 1–6 Å was consistent with that of the typical Zr MOF-801[33], confirming the

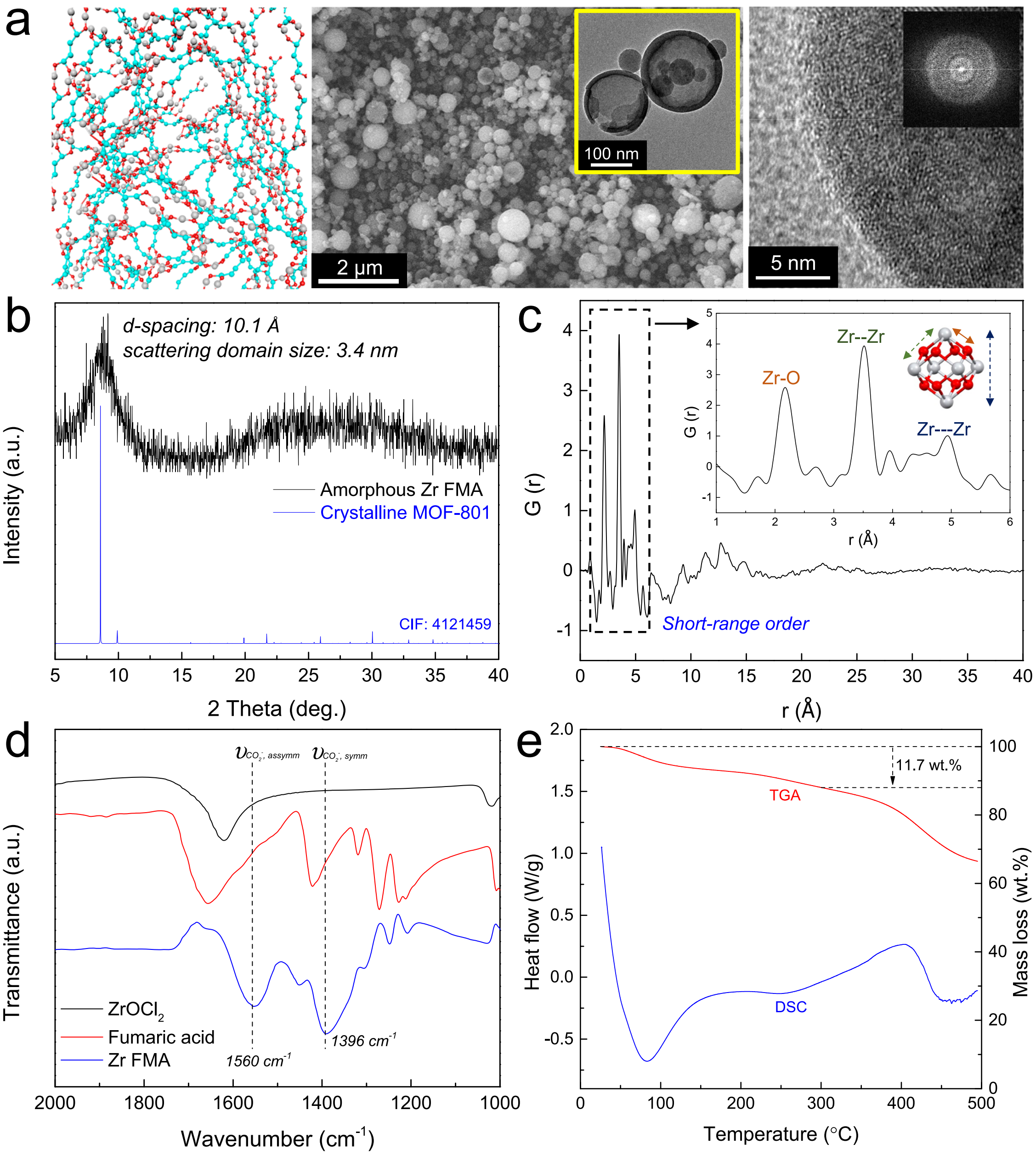

Fig. 4 | Flame-synthesized amorphous MOF, Zr FMA. a Structural schematic, SEM, TEM, HRTEM, and FFT images; **b** XRD pattern of Zr FMA; **c** PDF pattern of Zr FMA. The gray atom is Zr and red atom is O in the schematic; **d** FTIR spectra of $ZrOCl_2$, fumaric ligand, and Zr FMA; **e** TGA and DSC analysis. Additional amorphous MOFs and their characterization are shown in Supplementary Figs. 10–27.

local structure of Zr_6O_8 nodes. The inset in Fig. 4c illustrates the interatomic distances for the first 3 peaks of the PDF, in the context of the Zr_6O_8 oxoclusters that are the building blocks of Zr MOF-801. Despite the absence of long-range order in the amorphous MOF, metal ions and organic molecules remained interconnected. Formation of coordination bonds between Zr ions and the carboxylate linker was evident in FTIR spectra (Fig. 4d), where two new absorbance peaks appeared at 1396 and 1560 cm^{-1} corresponding to symmetric and asymmetric stretches of the Zr-coordinated carboxylate groups[34]. The presence of fumaric acid linker was also confirmed by ^1H NMR, via the proton resonance peak on C=C at 6.5 ppm (Supplementary Fig. 13). XPS analysis of amorphous Zr FMA matched that of crystalline MOF-801 (Supplementary Fig. 14). The amorphous Zr FMA exhibited a type I isotherm with a BET surface area of only 79 m^2/g and Langmuir surface area of 106 m^2/g, along with broad distribution of micropore sizes, ranging from 6 to 20 Å (Supplementary Fig. 15). The TGA analysis of amorphous Zr FMA in air (Supplementary Fig. 16) showed a similar mass loss to that of the typical crystalline Zr MOF-801[35,36], consistent with the similar stoichiometry.

To date, amorphous MOFs and MOF-like structures have been limited to a few types, primarily produced by amorphization of azolate and cyanide-based crystalline materials[15,37]. In the current non-equilibrium flame aerosol process, the rapid coordination between metal ions and organic linkers offers a direct pathway to amorphous MOFs. To demonstrate this point, we prepared a library of amorphous MOFs and related structures, including Zr UiO-66-NH_2, Fe FMA, Mg DHTA, Cu DHTA, Zr BTC, Zr BPDC, Fe BDC-NH_2 and Hf NDC (Supplementary Table 2). This set includes building block pairs for which amorphous MOFs have not previously been reported[15]. XRD patterns confirmed the amorphous nature of all samples, without distinct diffraction peaks (Supplementary Fig. 17). Meanwhile, the FTIR spectra of all the amorphous MOFs showed formation of new bonds compared to their reactants (Supplementary Fig. 18), demonstrating coordination between the clusters and the organic linkers[38]. SEM images showed sub-micrometer spherical particles, including both hollow and solid morphologies for each amorphous MOF (Supplementary Fig. 19). TEM images also showed uniform hollow or solid spheres with a smooth surface and no observable crystallinity or grain boundaries (Supplementary Fig. 20).

Specifically, the amorphous UiO-66-NH_2 (Zr + 2-Aminobenzene-1,4-dicarboxylic acid) was characterized in detail. HRTEM imaging and corresponding FFT images showed the random atomic arrangement and random distribution of micropores within the framework (Supplementary Fig. 21). PDF analysis revealed short-range order in amorphous UiO-66-NH_2, with major peaks appearing below 5 Å (Supplementary Fig. 22). The PDF pattern in the medium distance range of 0–20 Å (Supplementary Fig. 23a) was consistent with the previously reported amorphous Zr UiO-66 MOF. At shorter range of 1–6 Å (Supplementary Fig. 23b), the pattern is consistent with both crystalline and amorphous Zr UiO-66 MOFs[39]. This confirms the amorphous nature of the flame-synthesized UiO-66-NH_2 MOF and the presence of Zr_6O_8 clusters as its building blocks. Additionally, the XPS matched that of crystalline UiO-66-NH_2 (Supplementary Fig. 24). Thermogravimetric analysis (TGA) was conducted on amorphous Zr FMA and Zr UiO-66-NH_2 MOFs under N_2 atmosphere (Fig. 4e, Supplementary Fig. 25). Both exhibited high thermal stability, and the mass loss of amorphous UiO-66-NH_2 was only 6.3 wt.% at 300 °C, corresponding to the removal of adsorbed H_2O. Meanwhile, the main bridging bonds in the amorphous Zr FMA and Zr UiO-66-NH_2 were retained after sintering at 300 °C for 3 hours Supplementary Fig. 26), further indicating their robust thermal stability. In addition, differential scanning calorimetry (DSC) analysis revealed no apparent glass transition temperature (T_g) for the two amorphous MOFs (Fig. 4e, Supplementary Fig. 25). The MOFs remained amorphous after heating at 300 °C and 400 °C for 3 hours (Supplementary Fig. 27).

In-situ dispersion of single atoms/bimetallic MOFs

Besides forming nanocrystalline MOFs and amorphous MOFs, another groundbreaking advantage of rapid far-from-equilibrium synthesis is its ability to achieve a homogeneous distribution of building units, thereby integrating different metal species into a single phase. This method transcends traditional equilibrium-based approaches that are limited to chemically similar metal ions. For example, our previous study demonstrates that the non-equilibrium flame aerosol process can incorporate immiscible elements in a single-phase metal oxide[40,41]. Here, the flame aerosol approach also allows integration of very different metal species into a single (metastable) MOF phase, even when a homogeneous distribution (mixing) of the metal ions is not thermodynamically favorable. Figure 5a illustrates this process: two metal species dissolved in a precursor solution remain distinct after atomization. During rapid droplet evaporation, these metal ions simultaneously bond to organic linkers, a step that occurs much faster than the gradual MOF crystallization in near-equilibrium processes. The swift nature of droplet-to-particle conversion under far-from-equilibrium conditions prevents the building units from segregating into separate MOF crystals, allowing diverse metal ions to be kinetically trapped within a single MOF phase. Rapid quenching preserves the metastable bimetallic single MOF phase. Consequently, atomically dispersed active sites are incorporated directly into the MOF matrix, forming MOF-supported single-atom catalysts.

This non-equilibrium synthesis route circumvents the limitations set by thermodynamically favorable arrangements. Thus, it provides a versatile pathway for embedding single-atom active sites into MOF supports or creating heterometallic sites within MOFs. To demonstrate the power and generality of this approach, we randomly doped four active metals in MOFs, including single-atom Au in crystalline Cu HKUST-1 MOF, single-atom Co in crystalline Ni PBA MOF, single-atom Pt in amorphous UiO-66-NH_2 MOF, and single-atom Pd in amorphous Zr FMA MOF. The concentration of active metals can be flexibly adjusted. Inductively coupled plasma optical emission spectroscopy (ICP-OES) measured Au, Co, Pt, and Pd content in these MOFs of 2.0 wt.%, 12.5 wt.%, 4.3 wt.%, and 4.7 wt.%, respectively. The molar ratios of the two metals in the bimetallic MOF products are shown in Supplementary Table 13. Given that Co and Ni share similar properties and both Co PBA and Ni PBA exhibit the same cubic FCC structure, the Co-Ni PBA exhibited an elemental ratio in the final product very close to that in the precursor solution. However, in other bimetallic MOFs, due to the differences in the physicochemical properties of the two metal elements, the ratio of elements in the final product deviated from the ratio provided in the precursor. HAADF-STEM maps revealed the homogeneous distribution of M1, M2, and C in all the materials (Fig. 5b–e), indicating that the secondary metals were incorporated into the host matrix in each case. Moreover, after introducing the secondary metals, the XRD patterns remained the same as those of the parent MOFs, without any additional metallic or metal oxide peaks (Supplementary Fig. 28). TEM and HRTEM images further confirmed this result, as agglomeration and sintering of metal species were not observed (Fig. 5f, Supplementary Figs. 29 and 30). All characterizations collectively demonstrated the incorporation of atomically dispersed active sites into the MOFs.

To further investigate the microstructure of the doped metal species, aberration corrected scanning transmission electron microscopy (AC-STEM) was employed for the 4.3 wt.% Pt in amorphous Zr UiO-66-NH_2 (Fig. 5g). Isolated Pt atoms were clearly seen as randomly dispersed bright spots, with no observable aggregated Pt nanoparticles. Moreover, X-ray absorption spectroscopy (XAS) was performed to determine the coordination environment of Pt species. The intense edge feature, often referred to as white line, originates from $2p_{3/2}\rightarrow 5d$ electron transition. The intensity of the white line is strongly correlated with the oxidation state, where higher occupancy of the 5d state results in less intense white line. The XANES white line intensity for Pt in amorphous UiO-66-NH_2 was higher than that of Pt foil, indicating oxidized Pt states (Fig. 5h). This was consistent with the Pt $4f$ XPS spectrum, revealing the predominant existence of Pt^{2+}, with no detection of Pt^0 (Supplementary Fig. 31). The Fourier-transform extended X-ray absorption fine structure (EXAFS) spectrum displayed the Pt-O bond formed by the coordination of Pt cations with carboxyl groups in BDC-NH_2 linkers (Fig. 5i, Supplementary Table 14)[42]. No Pt-Pt bonding was evident, aligning with AC-STEM, elemental maps, and XRD results, demonstrating the homogeneous dispersion of isolated Pt atoms within the MOF matrix.

Incorporating such atomically dispersed heterometals in MOFs is desirable in catalysis, where single-atom and bimetallic active sites can effectively modulate catalyst activity and selectivity. Coordination of metal atoms to ligands can provide strong metal-support interactions to improve catalyst stability[18]. This category of catalyst has demonstrated promise in numerous reactions, including gas-phase reactions such as water-gas shift[42] and propane dehydrogenation[43] reactions; organic synthesis such as ethylene dimerization[44] and domino coupling[45] reactions; and photocatalytic reactions such as H_2 evolution[46]. In electrocatalysis, the bimetallic MOFs can be directly used for processes including CO_2 reduction[47], or can be pyrolyzed into oxide or carbon supported single-atom catalysts, such as the ZIF-derived Ir-Co_3O_4 for OER[48] and Fe-N-C catalyst for ORR[49] reactions.

Exsolution of active nanoclusters and application in CO oxidation

In addition to directly using the flame synthesized MOF-based single atom catalysts/bimetallic MOFs, the secondary metal can be further exsolved by reduction, forming MOF-supported nanocatalysts. As shown in Fig. 6a, the 4.3 wt.% Pt in amorphous Zr UiO-66-NH_2 was reduced by $NaBH_4$ in solution. Reduction of Pt cations drove

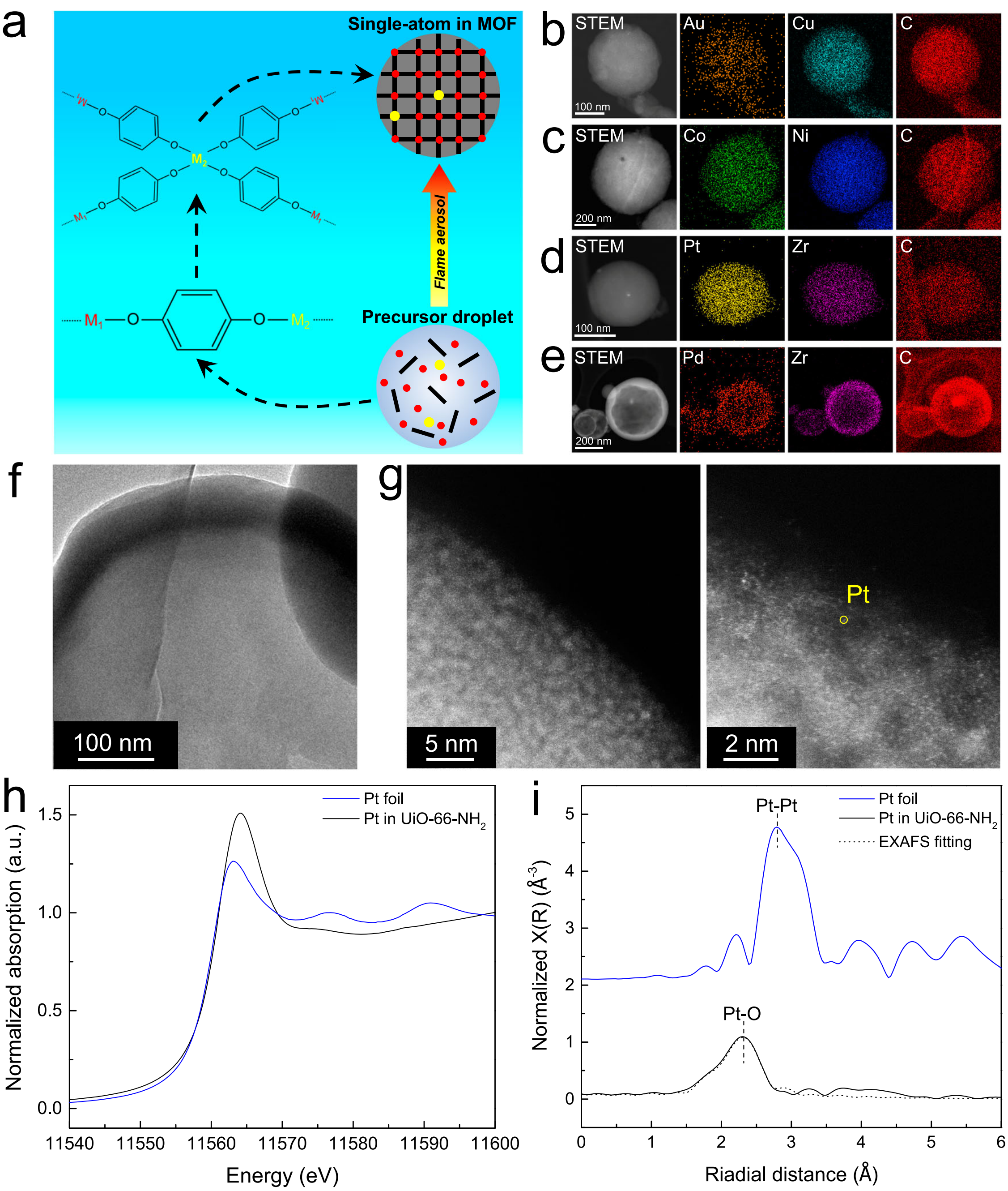

Fig. 5 | Kinetic dispersion of single atoms. a Schematic of in-situ doping of single-atom active sites in a MOF matrix in a non-equilibrium flame aerosol process; HAADF-STEM elemental maps of **b** single atom Au in Cu HKUST-1; **c** single atom Co in Ni PBA; **d** single atom Pt in amorphous Zr UiO-66-NH_2; **e** single atom Pd in amorphous Zr FMA; **f** TEM image; **g** AC-STEM image; **h** XANES spectra at the Pt L_3-*edge* and **i** the k^2-weighted Fourier transform of Pt L_3-*edge* EXAFS spectra of single-atom Pt in amorphous Zr UiO-66-NH_2 MOF.

exsolution of Pt out of the UiO-66-NH_2 matrix to form metallic Pt anchored to the MOF. HAADF-STEM and elemental mapping revealed ultra-small Pt nanoclusters on UiO-66-NH_2 after reduction (Fig. 6b). The XRD pattern confirmed the phase-separation by the appearance of small metallic Pt diffraction peaks (Supplementary Fig. 32). Before reduction, only Pt-O bonds were detected by EXAFS, indicating the presence of atomic Pt ions in UiO-66-NH_2. After reduction, all the Pt-O bonds were gone, and only Pt-Pt bonds were observed (Fig. 6c, Supplementary Fig. 33, Supplementary Table 14). The Pt *4f* XPS spectrum also revealed Pt^0 (Supplementary Fig. 34). The proposed exsolution behavior generated highly dispersed active nanoclusters. The average size of exsolved Pt nanoparticles was only 2.84 nm with a high loading of 4.3 wt.% (Fig. 6d). Moreover, this exsolution phenomenon is a general mechanism. Reducible elements such as Pt, Pd, Au, Ir, Ni, Cu, and others can first be incorporated into MOFs based on irreducible metals like Zr, Hf, Ce, Tb, Al, or Mg using the flame aerosol process. These composites serve as precursors for subsequent exsolution, significantly broadening the scope for innovative material design aimed at diverse applications. For example, Pd nanoparticles also can be exsolved from Pd-Zr UiO-66-NH_2 and Pd-Zr FMA by the same processes, which exhibited similar ultra-small particle size and uniform dispersion (Supplementary Fig. 35).

MOF-supported active metal nanoclusters are promising catalysts for many reactions[18]. As a prototypical example, we tested one of them for low-temperature CO oxidation[50] (CO lean combustion). This served as a model reaction to test the Pt/UiO-66-NH_2 catalysts. For this, we

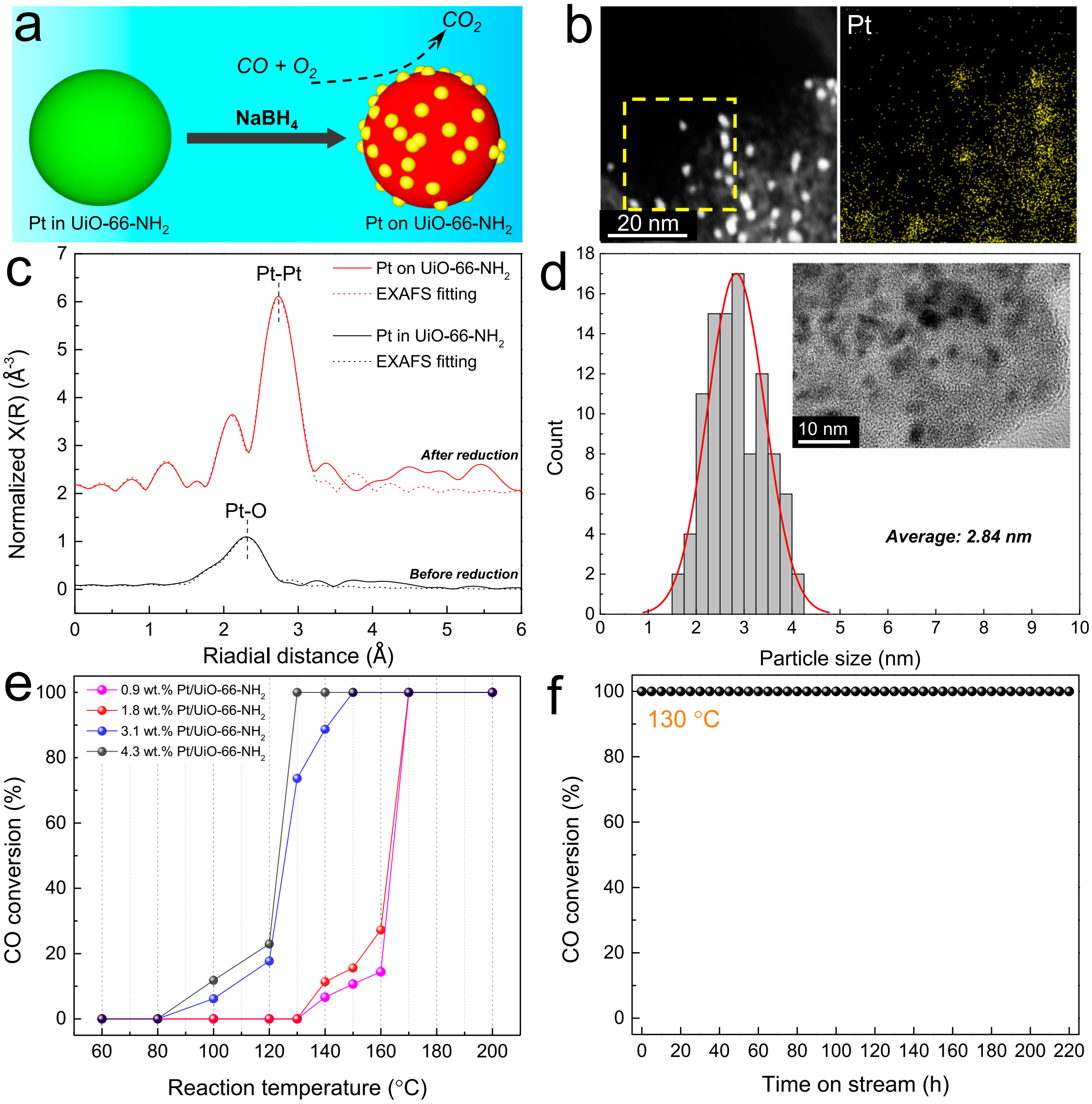

Fig. 6 | Exsolution behavior and catalytic performance. **a** Schematic of Pt exsolution and application in CO oxidation; **b** HAADF-STEM elemental map of Pt nanoclusters on amorphous Zr UiO-66-NH_2; **c** The k^2-weighted Fourier transforms of Pt *L_3-edge* EXAFS spectra of single atom Pt in amorphous Zr UiO-66-NH_2 and Pt/UiO-66-NH_2; **d** HRTEM image and particle size distribution of Pt/UiO-66-NH_2, statistics of 100 Pt nanoparticles from HRTEM images; **e** Activity analysis of Pt/UiO-66-NH_2 as a heterogeneous catalyst for CO oxidation reaction at varied temperatures with different Pt content and **f** long-term stability test of 4.3 wt.% Pt/UiO-66-NH_2 catalyst at 130 °C for 220 hours.

monitored CO conversion as reaction temperature increased from 60 to 200 °C (Fig. 6e), i.e., measured light-off curves. The CO conversion increased with rising reaction temperature, and CO light-off temperatures decreased with increasing Pt content. The 4.3 wt.% Pt/UiO-66-NH_2 achieved 100% CO conversion at 130 °C, demonstrating its high activity for this reaction. The stability of the 4.3 wt.% Pt/a-UiO-66-NH_2 catalyst was verified by a time-on-stream test at 130 °C, maintaining constant 100% CO conversion for more than 220 hours (Fig. 6f). This catalytic performance demonstrated far exceeds the United States Department of Energy (DOE) target for achieving more than 90% CO conversion below 150 °C[51].

Discussion

This research establishes a non-equilibrium flame aerosol methodology to fabricate MOFs. The rapid droplet-to-particle conversion process provides a general route to prepare both nanocrystal MOFs and amorphous MOFs. Meanwhile, it enables incorporation of otherwise incompatible metal ions in a single MOF phase. The resulting bimetallic MOFs exhibit many desirable characteristics such as atomically dispersed active sites and flexible composition. They can be directly applied in their as-synthesized metastable state or serve as exsolution precursors for nano-phase separation. The intrinsic scalability, single-step continuous operation, and relatively low cost of the aerosol process make it ideal for industrial production, potentially leading to the widespread development and application of nanocrystalline and amorphous MOFs in fields such as membrane separations, sensors, and catalysis.

Methods

Chemicals

$Cu(NO_3)_2{\bullet}2.5H_2O$ (98 + %, Acros Organics), $Tb(NO_3)_3{\bullet}H_2O$ (99.99%, Thermo Scientific), $Ni(NO_3)_2{\bullet}6H_2O$ (99%, Acros Organics), $Zn(NO_3)_2{\bullet}6H_2O$ (98%, Sigma Aldrich), $ZrOCl_2{\bullet}8H_2O$ (98%, Alfa Aesar), $ZrCl_4$ (99.5%, Alfa Aesar), $FeCl_2{\bullet}4H_2O$ (99%, Acros Organics), $Mg(NO_3)_2{\bullet}6H_2O$ (99 + %, Acros Organics), $HfCl_4$ (99.9%, Alfa Aesar), $AuCl_3$ (99%, Thermo Scientific), $Co(NO_3)_2{\bullet}6H_2O$ (99%, Acros Organics),

$Pd(NO_3)_2{\bullet}H_2O$ (39 wt.% Pd, Thermo Scientific), $Pt(NO_3)_4$ solution (15 wt.% Pt, Thermo Scientific), 1,3,5-benzenetricarboxylic acid (BTC, 98%, Thermo Scientific), 1,4-benzenedicarboxylic acid (BDC, 99%, Thermo Scientific), 1,4-phenylenediacetic acid (PDA, 97%, Thermo Scientific), fumaric acid (FMA, 99%, Thermo Scientific), potassium ferricyanide ($K_3Fe(CN)_6$, 99%, Thermo Scientific), 2-aminobenzene-1,4-dicarboxylic acid (BDC-NH_2, 99%, Thermo Scientific), pyromellitic acid (PMA, 96%, Thermo Scientific), 1,3,5-tris(4-carboxyphenyl) benzene (BTB, 97%, Thermo Scientific), 2,5-dihydroxyterephthalic acid (DHTA, 97%, Thermo Scientific), biphenyl-4,4′-dicarboxylic acid (BPDC, 98%, Acros Organics), 2,6-naphthalenedicarboxylic acid (NDC, 98%, Thermo Scientific), sodium borohydride ($NaBH_4$, 98%, Thermo Scientific), N,N-dimethylformamide (DMF, 99.8%, Fisher Chemical), formic acid (88%, Aqua Solutions), ethanol (200 proof, Decon), and methanol (Sigma Aldrich) were used as received.

Flame aerosol synthesis of MOFs

The precursor solution was prepared by dissolving inorganic metal salt and organic ligands in a solvent or solvent mixture that was compatible with both metal and ligand. Detailed precursor solution compositions for nanocrystal MOFs are shown in Supplementary Table 1 and for amorphous MOFs are shown in Supplementary Table 2. In cases in which the metal ion and organic ligand form precipitated in the solution, they were instead dissolved in separate containers and simultaneously injected into the reactor. The mixing occurred at a connector near the point of injection, and the mixing time was too short to allow precipitation before atomization. To prevent the precursor solution from igniting, a mixture of organic solvent and water was used as the solvent to ensure solubility of all precursor components without using a flammable solvent mixture. The ratio of metal cations to organic ligands in the precursor was designed based on typical MOF structures and conventional synthesis methods. For example, in the synthesis of Cu HKUST-1 ($Cu_3(BTC)_2$), $Cu(NO_3)_2$ and 1,3,5-benzenetricarboxylic acid in a 3:2 molar ratio were dissolved in a mixture of DMF, EtOH, and H_2O. In the flame reactor, an inverted diffusion flame was generated by igniting a gas mixture of 3.5 L/min H_2, 10 L/min N_2, and 4 L/min O_2, yielding a temperature of ~400 °C in the reactor chamber. The reaction temperature can be varied by increasing or decreasing the H_2 gas flow rate. Nitrogen supplied to the flame along with the hydrogen fuel serves to increase the overall gas flow rate and limit the peak flame temperature. The overall gas flow rate should be high enough to achieve sonic velocity within the nozzle that separates the flame from the reaction chamber. The overall gas flow rate also determines the residence time of the MOF product in the high-temperature reaction chamber. Note that the temperature in the reaction chamber is far below the adiabatic flame temperature due to heat losses to the surroundings as well as cooling due to expansion and precursor solution evaporation. Gases after combustion (N_2, water vapor, and excess O_2) passed through a converging-diverging nozzle (drill Ø0.1111 inch, #34), forming a sonic velocity hot stream. The precursor solution was injected into the throat section of the converging-diverging nozzle (drill Ø0.1040 inch, #37) by a peristaltic pump at 250 mL/h flow rate. In this case, the precursor solution was instantly atomized into microdroplets. The precursor droplets evaporated instantly, and spherical MOF particles formed from each droplet. Downstream of the reactor chamber, the produced MOF particles were immediately quenched by a 140 L/min N_2 flow to stabilize the MOF structures and prevent particle agglomeration or sintering. Then, the product was collected on a PVDF filter membrane. A downstream vacuum pump provided the pressure drop to maintain flow through the membrane and remove the exhaust gases (N_2, water vapor, O_2, and a small amount of NO_2). The produced powder was re-dispersed in 30 mL solvent, sonicated for 1 hour, and soaked for over 5 hours at room temperature before being centrifuged. It was washed twice with DMF and once with methanol. Finally, the sample was vacuum-dried at 60 °C overnight. The production yield of MOFs is 0.3–1 g of washed product per hour of reactor operation. The closed reactor system used in this study allows any harmful gases generated in the reaction to be vented via the building chemical exhaust system. It also isolates the flame and the reaction chamber from the surroundings. In a commercial-scale implementation, a scrubber might be required to remove any byproducts (NO_x) from the exhaust gas stream.

In-situ incorporation of single-atoms/synthesis of bimetallic MOFs

All the procedures for fabricating MOF-based single-atom catalysts (or bimetallic MOFs) were identical to those for single-metal MOFs, apart from adding a second metal salt in the precursor solution.

Exsolution of active nanoclusters

In a typical experiment, 100 mg flame synthesized Pt-Zr UiO-66-NH_2 and 400 mg $NaBH_4$ were combined in 30 mL ethanol and stirred at 60 °C for 4 hours. Then, the sample was collected by centrifugation and washed with ethanol twice. Finally, the sample was dried in air at 100 °C overnight.

Material characterizations

X-ray diffraction (XRD) patterns were measured using an X-ray diffractometer (Rigaku Ultima IV) with Cu Kα source ($\lambda = 0.15418$ nm); High-angle annular dark-field scanning transmission electron microscopy (HAADF-STEM) imaging with elemental mapping by energy-dispersive x-ray spectroscopy (EDS), and live fast-Fourier-transform (FFT) patterns were obtained using a JEOL 2100-F 200 kV field-emission analytical transmission electron microscope; Aberration corrected scanning transmission electron microscopy (AC-STEM) images were measured by a modified FEI Titan 80-300 microscope; A JEOL JEM 2010 Transmission Electron Microscope (TEM) and a Cross-Beam Focused Ion Beam-Scanning Electron Microscopy (FIB-SEM) Workstation (Carl Zeiss AURIGA) were also used to observe the product particle morphology; The ex-situ X-ray absorption spectroscopy (XAS) Pt *L3-edge* spectra were collected at 8-ID beamline (Inner Shell Spectroscopy) of Brookhaven Lab's National Synchrotron Light Source II. The measurements were carried out in fluorescence mode; The PDF measurements were carried out at 28-ID-2 beamline of National Synchrotron Light Source II (NSLS II) at Brookhaven National Laboratory (BNL), using a photon wavelength of 0.18475 Å and a 2D detector (2k × 2k pixel). Each sample was measured for 10 min to obtain high-quality data. N_2 sorption isotherms were measured using a Micromeritics 3Flex adsorption analyzer. The samples were degassed at 120 °C for 10 h prior to analysis to remove moisture. The specific surface area was calculated based on the Brunauer-Emmett-Teller (BET) and Langmuir methods, and the pore size distribution was calculated by the Horvath-Kawazoe method; Nuclear magnetic resonance (1H NMR) spectra were acquired on a Bruker Neo-400 spectrometer. Prior to 1H NMR analysis, the MOFs were digested in a mixture of 35% DCl in D_2O and deuterated dimethyl sulfoxide (DMSO-d6); Fourier transform infrared (FTIR) spectra were collected using a Bruker Vertex 70 spectrometer; X-ray photoelectron spectroscopy (XPS) measurements were conducted on a Thermo Fisher K-Alpha Plus instrument. The photoelectron spectrometer system was configured with an Al Kα excitation source with spot size of 400 µm; TGA was performed on a DSC SDT Q600 from TA Instruments. The samples were heated from 25 °C to 500 °C in N_2 at a temperature ramp rate of 10 °C/min; An inductively coupled plasma optical emission spectrometer (ICP-OES, Thermo Scientific iCAP 6000) was used to determine the single-atom active metal content in MOFs.

Catalyst tests

Catalyst performance for CO oxidation reaction was measured using a continuous fixed-bed flow reactor at atmospheric pressure. A mixture of 50 mg catalyst with 200 mg sand was packed into quartz tube. Reactant gases comprising 4% CO, 20% O_2, and 76% Ar were fed at 50 mL/min flow rate, with a gas hourly space velocity (GHSV) of 60,000 mL/(g_{cat}•h). The reaction temperature was increased from 60 to 200 °C. The effluent gases were analyzed online by a gas chromatograph (SRI 8610) fitted with a packed column (Restek Natural Gas ShinCarbon ST) and a thermal conductivity detector (TCD). The CO conversion was calculated by Eq. (1):

$$X_{CO} = \frac{F_{in,CO} - F_{out,CO}}{F_{in,CO}} \times 100\% \tag{1}$$

Data availability

Additional data that support the findings of this study are reported in the Supplementary Information. All the data are available from corresponding authors upon request.

References

1. Furukawa, H., Cordova, K. E., O'Keeffe, M. & Yaghi, O. M. The chemistry and applications of metal-organic frameworks. *Science* **341**, 1230444 (2013).
2. Stanley, P. M., Haimerl, J., Shustova, N. B., Fischer, R. A. & Warnan, J. Merging molecular catalysts and metal-organic frameworks for photocatalytic fuel production. *Nat. Chem.* **14**, 1342–1356 (2022).
3. Han, X., Yang, S. H. & Schröder, M. Porous metal-organic frameworks as emerging sorbents for clean air. *Nat. Rev. Chem.* **3**, 108–118 (2019).
4. Knebel, A. & Caro, J. Metal-organic frameworks and covalent organic frameworks as disruptive membrane materials for energy-efficient gas separation. *Nat. Nanotechnol.* **17**, 911–923 (2022).
5. Yang, J. & Yang, Y. W. Metal–organic frameworks for biomedical applications. *Small* **16**, 1906846 (2020).
6. Koo, W.-T., Jang, J.-S. & Kim, I.-D. Metal-organic frameworks for chemiresistive sensors. *Chem* **5**, 1938–1963 (2019).
7. Hanikel, N., Prevot, M. S. & Yaghi, O. M. MOF water harvesters. *Nat. Nanotechnol.* **15**, 348–355 (2020).
8. Koirala, R., Pratsinis, S. E. & Baiker, A. Synthesis of catalytic materials in flames: opportunities and challenges. *Chem. Soc. Rev.* **45**, 3053–3068 (2016).
9. Liu, S., Mohammadi, M. M. & Swihart, M. T. Fundamentals and recent applications of catalyst synthesis using flame aerosol technology. *Chem. Eng. J.* **405**, 126958 (2021).
10. Ensor, D. S. Aerosol science and technology: history and reviews, (RTI Press, 2011).
11. Barros, B. S., Neto, O. J. D., Fros, A. C. D. & Kulesza, J. Metal-organic framework nanocrystals. *ChemistrySelect* **3**, 7459–7471 (2018).
12. Dai, S. et al. Highly defective ultra-small tetravalent MOF nanocrystals. *Nat. Commun.* **15**, 3434 (2024).
13. Marshall, C. R., Staudhammer, S. A. & Brozek, C. K. Size control over metal-organic framework porous nanocrystals. *Chem. Sci.* **10**, 9396–9408 (2019).
14. Madsen, R. S. et al. Ultrahigh-field 67Zn NMR reveals short-range disorder in zeolitic imidazolate framework glasses. *Science* **367**, 1473–1476 (2020).
15. Ma, N. & Horike, S. Metal-organic network-forming glasses. *Chem. Rev.* **122**, 4163–4203 (2022).
16. Yang, Z. et al. ZIF-62 glass foam self-supported membranes to address CH_4/N_2 separations. *Nat. Mater.* **22**, 888–894 (2023).
17. Fonseca, J., Gong, T., Jiao, L. & Jiang, H.-L. Metal–organic frameworks (MOFs) beyond crystallinity: amorphous MOFs, MOF liquids and MOF glasses. *J. Mater. Chem. A* **9**, 10562–10611 (2021).
18. Liu, L. & Corma, A. Confining isolated atoms and clusters in crystalline porous materials for catalysis. *Nat. Rev. Mater.* **6**, 244–263 (2020).
19. Wei, Y. S., Zhang, M., Zou, R. Q. & Xu, Q. Metal-organic framework-based catalysts with single metal sites. *Chem. Rev.* **120**, 12089–12174 (2020).
20. Liu, S. et al. A general route to flame aerosol synthesis and in situ functionalization of mesoporous silica. *Angew. Chem.-Int. Edit.* **61**, e202206870 (2022).
21. Liu, S. et al. Producing ultrastable Ni-ZrO_2 nanoshell catalysts for dry reforming of methane by flame synthesis and Ni exsolution. *Chem. Catalysis* **2**, 1–13 (2022).
22. Zhao, H., Wu, Z. W., Li, W. F., Xu, J. L. & Liu, H. F. Transition Weber number between surfactant-laden drop bag breakup and shear breakup of secondary atomization. *Fuel* **221**, 138–143 (2018).
23. Kastengren, A. et al. Measurements of droplet size in shear-driven atomization using ultra-small angle x-ray scattering. *Int. J. Multiph. Flow.* **92**, 131–139 (2017).
24. Liu, S. et al. Flame aerosol synthesis of hollow alumina nanoshells for application in thermal insulation. *Chem. Eng. J.* **428**, 131273 (2022).
25. Eslamian, M., Ahmed, M. & Ashgriz, N. Modeling of solution droplet evaporation and particle evolution in droplet-to-particle spray methods. *Dry. Technol.* **27**, 3–13 (2009).
26. Chui, S. S.-Y., Lo, S. M.-F., Charmant, J. P., Orpen, A. G. & Williams, I. D. A chemically functionalizable nanoporous material $[Cu_3(TMA)_2(H_2O)_3]_n$. *Science* **283**, 1148–1150 (1999).
27. Babu, D. J. et al. Restricting lattice flexibility in polycrystalline metal-organic framework membranes for carbon capture. *Adv. Mater.* **31**, 1900855 (2019).
28. Cai, X., Xie, Z., Pang, M. & Lin, J. Controllable synthesis of highly uniform nanosized HKUST-1 crystals by liquid–solid–solution method. *Cryst. Growth Des.* **19**, 556–561 (2019).
29. Lu, P., Qi, Z. Y., Chen, J., Ye, C. S. & Qiu, T. Enhancing adsorption desulfurization performance using enriched cu(i) sites over microenvironment-modulated HKUST-1. *Small* **49**, 2304644 (2023).
30. Zhao, Y., Lee, S. Y., Becknell, N., Yaghi, O. M. & Angell, C. A. Nanoporous transparent MOF glasses with accessible internal surface. *J. Am. Chem. Soc.* **138**, 10818–10821 (2016).
31. Sapnik, A. F. et al. Mixed hierarchical local structure in a disordered metal-organic framework. *Nat. Commun.* **12**, 2062 (2021).
32. Bennett, T. D. et al. Structure and properties of an amorphous metal-organic framework. *Phys. Rev. Lett.* **104**, 115503 (2010).
33. Ma, R. et al. Transition from isotropic positive to negative thermal expansion by local Zr_6O_8 node distortion in MOF-801. *Microstructures* **4**, 2024023 (2024).
34. Hashjin, M. A., Zarshad, S., Emrooz, H. B. M. & Sadeghzadeh, S. Enhanced atmospheric water harvesting efficiency through green-synthesized MOF-801: a comparative study with solvothermal synthesis. *Sci. Rep.* **13**, 16983 (2023).
35. Liu, H. et al. Investigation on a Zr-based metal-organic framework (MOF-801) for the high-performance separation of light alkanes. *Chem. Commun.* **57**, 13008–13011 (2021).
36. Muthu Prabhu, S., Kancharla, S., Park, C. M. & Sasaki, K. Synthesis of modulator-driven highly stable zirconium-fumarate frameworks and mechanistic investigations of their arsenite and arsenate adsorption from aqueous solutions. *CrystEngComm* **21**, 2320–2332 (2019).
37. Wei, Y.-S., Fan, Z., Luo, C. & Horike, S. Desolvation of metal complexes to construct metal–organic framework glasses. *Nat. Synth.* **3**, 214–223 (2023).
38. Xu, W. et al. High-porosity metal-organic framework glasses. *Angew. Chem. Int. Ed.* **62**, e202300003 (2023).
39. Bennett, T. D. et al. Connecting defects and amorphization in UiO-66 and MIL–140 metal-organic frameworks: a combined experimental and computational study. *Phys. Chem. Chem. Phys.* **18**, 2192–2201 (2016).
40. Liu, S. et al. Challenging thermodynamics: combining immiscible elements in a single-phase nano-ceramic. *Nat. Commun.* **15**, 1167 (2024).

41. Liu, S. et al. A general flame aerosol route to high-entropy nanoceramics. *Matter* **7**, 1–20 (2024).
42. Rivero-Crespo, M. A. et al. Confined Pt(1) (1+) water clusters in a MOF catalyze the low-temperature water-gas shift reaction with both CO(2) oxygen atoms coming from water. *Angew. Chem. Int. Ed.* **57**, 17094–17099 (2018).
43. Li, Z. Y. et al. Metal-organic framework supported cobalt catalysts for the oxidative dehydrogenation of propane at low temperature. *ACS Central Sci.* **3**, 31–38 (2017).
44. Metzger, E. D., Comito, R. J., Hendon, C. H. & Dincă, M. Mechanism of single-site molecule-like catalytic ethylene dimerization in Ni-MFU-4 l. *J. Am. Chem. Soc.* **139**, 757–762 (2017).
45. Zhang, X. i Xamena, F.L. & Corma, A. Gold (III)–metal organic framework bridges the gap between homogeneous and heterogeneous gold catalysts. *J. Catal.* **265**, 155–160 (2009).
46. Zuo, Q. et al. Ultrathin metal–organic framework nanosheets with ultrahigh loading of single Pt atoms for efficient visible-light-driven photocatalytic H_2 evolution. *Angew. Chem. Int. Ed.* **58**, 10198–10203 (2019).
47. Kornienko, N. et al. Metal–organic frameworks for electrocatalytic reduction of carbon dioxide. *J. Am. Chem. Soc.* **137**, 14129–14135 (2015).
48. Shan, J. et al. Short-range ordered iridium single atoms integrated into cobalt oxide spinel structure for highly efficient electrocatalytic water oxidation. *J. Am. Chem. Soc.* **143**, 5201–5211 (2021).
49. Zeng, Y. et al. Tuning the thermal activation atmosphere breaks the activity–stability trade-off of Fe–N–C oxygen reduction fuel cell catalysts. *Nat. Catal.* **6**, 1215–1227 (2023).
50. Freund, H. J., Meijer, G., Scheffler, M., Schlögl, R. & Wolf, M. CO oxidation as a prototypical reaction for heterogeneous processes. *Angew. Chem. Int. Ed.* **50**, 10064–10094 (2011).
51. Rappé, K. G. et al. Aftertreatment protocols for catalyst characterization and performance evaluation: low-temperature oxidation, storage, three-way, and NH_3-SCR catalyst test protocols. *Emission Control Sci. Tech.* **5**, 183–214 (2019).
52. Yaghi, O. & Li, H. Hydrothermal synthesis of a metal-organic framework containing large rectangular channels. *J. Am. Chem. Soc.* **117**, 10401–10402 (1995).
53. Hermes, S., Zacher, D., Baunemann, A., Wöll, C. & Fischer, R. A. Selective growth and MOCVD loading of small single crystals of MOF-5 at alumina and silica surfaces modified with organic self-assembled monolayers. *Chem. Mat.* **19**, 2168–2173 (2007).
54. Carne-Sanchez, A., Imaz, I., Cano-Sarabia, M. & Maspoch, D. A spray-drying strategy for synthesis of nanoscale metal-organic frameworks and their assembly into hollow superstructures. *Nat. Chem.* **5**, 203–211 (2013).
55. Mueller, U. et al. Metal-organic frameworks -: prospective industrial applications. *J. Mater. Chem.* **16**, 626–636 (2006).
56. Sun, Y. J. & Zhou, H. C. Recent progress in the synthesis of metal-organic frameworks. *Sci. Technol. Adv. Mater.* **16**, 054202 (2015).
57. Rubio-Martinez, M. et al. New synthetic routes towards MOF production at scale. *Chem. Soc. Rev.* **46**, 3453–3480 (2017).
58. He, Q. et al. Recent progress of industrial preparation of metal–organic frameworks: synthesis strategies and outlook. *Mater. Today Sustain.* **17**, 100104 (2022).

Acknowledgements

This work at the University at Buffalo (SUNY) was supported by the DOE National Energy Technology Laboratory under Grant number DE-FE0032209. Work at the Molecular Foundry at Lawrence Berkeley National Laboratory was supported by the Office of Science, Office of Basic Energy Sciences of the U.S. DOE under Contract No. DE-AC02-05CH11231. This research used resources of the 8-ID (ISS) and 28-ID-2 (XPD) beamlines of the National Synchrotron Light Source II, a U.S. DOE Office of Science User Facility operated for the DOE Office of Science by Brookhaven National Laboratory under Contract no. DE-SC0012704.

Author contributions

S.L., C.C.D., and M.T.S. conceived the idea and the experiments. S.L. designed all the materials. S.L., K.L.T., and M.A.K. performed the materials synthesis. S.L. performed the catalysts measurements. S.L., C.C.D., F.P.Y., D.W., S.G., K.W.C., L.F.C., R.C., and Z.X.X. performed the materials characterizations. M.Y., J.J.U., and M.T.S. provided the resources. S.L. wrote the first manuscript draft. C.C.D., J.J.U, and M.T.S. revised the manuscript. C.C.D., J.J.U, and M.T.S. jointly supervised this work.

Competing interests

The authors declare no competing interests.

Additional information

Supplementary information The online version contains supplementary material available at https://doi.org/10.1038/s41467-024-53678-4.

Correspondence and requests for materials should be addressed to Chaochao Dun, Jeffrey J. Urban or Mark T. Swihart.

Peer review information *Nature Communications* thanks Antoine Tissot, and the other, anonymous, reviewer(s) for their contribution to the peer review of this work. A peer review file is available.